nature communications

Article

https://doi.org/10.1038/s41467-025-57604-0

Sub-minute synthesis and modulation of β/λ-$M_xTi_{3-x}O_5$ ceramics towards accessible heat storage

Received: 23 May 2024

Accepted: 14 February 2025

Published online: 11 March 2025

Check for updates

Pengfei Zhao[1,5], Guangshi Li[1,2,5] ✉, Xiaolu Xiong[1,3] ✉, Peng Cheng[1], Zhongya Pang[1,2], Chenteng Sun[1,2], Hu Cheng[4], Caijuan Shi[4], Xing Yu[1,2], Qian Xu[1,2], Xingli Zou[1,2] ✉ & Xionggang Lu[1] ✉

Nearly 50% of global primary energy consumption is lost as low-temperature heat. λ-Ti_3O_5 holds promise for waste heat harvesting and reuse; however, achieving reversible phase transitions between its λ and β phases under accessible conditions remains a major challenge. Here, we proposed a simple laser method that incorporates element substitution for sub-minute synthesis (20–60 s) of λ-$M_xTi_{3-x}O_5$ (M = Mg, Al, Sc, V, Cr, Mn, or Fe, $0.09 \le x \le 0.42$). In particular, aluminum-substituted λ-$Al_xTi_{3-x}O_5$ demonstrated the lowest energy barrier, with a transition pressure of 557 MPa and temperature of 363 K. Notably, compression of the (001) crystal plane could reduce the transition pressure to only 35–40 MPa, enabling the applicability of λ-$Al_xTi_{3-x}O_5$ for wide applications in heat recovery and future lunar explorations.

More than 70% of the global primary energy consumption is lost during conversion, with nearly 50% being dissipated as low-temperature waste heat[1,2]. Moreover, directly recovering and reusing the waste heat has become a priority in recent years. λ-Ti_3O_5 has attracted significant attention in the fields of thermal energy utilization and conversion due to its unique physicochemical properties, such as photoinduced phase transition and light absorption[3,4]. Tokoro et al. reported a long-term heat-storage ceramic based on λ-Ti_3O_5 that exhibited intriguing reversible phase transitions between λ-Ti_3O_5 and β-Ti_3O_5[5]. The transition from λ-Ti_3O_5 to β-Ti_3O_5 can be induced by pressure, resulting in the release of heat. Conversely, the transition from the β-Ti_3O_5 to the λ-Ti_3O_5 can be induced by temperature variation, achieving effective heat storage. Notably, the pressure required for the λ→β phase transition is remarkably low (7–60 MPa)[6] compared to other materials[7–12], but the temperature required for the β→λ transition is relatively high (470–530 K). To further lower the phase transition temperature, a partially metal substitution of λ-Ti_3O_5 has been synthesized, i.e., λ-$M_xTi_{3-x}O_5$ (M = Sc or Mg), and it requires lower temperatures (311–353 K) for the β→λ phase transition[13,14]; however, its pressure for the λ→β phase transition increases to high pressure (680–2000 MPa). Therefore, achieving reversible phase transitions between the λ and β phases of Ti_3O_5 under an accessible low pressure and low temperature remains a challenge.

In this study, we propose a method called the laser-assisted vacuum smelting (LVS) process to achieve a sub-minute (20–60 s) synthesis of β-Ti_3O_5 and a series of metal-substituted λ-$M_xTi_{3-x}O_5$ (M = Mg, Al, Sc, V, Cr, Mn, or Fe, $0.09 \le x \le 0.42$) ceramics. The phase transition process of λ-$M_xTi_{3-x}O_5$ was then experimentally and theoretically studied, and the λ-$Al_xTi_{3-x}O_5$ was demonstrated to possess an accessible low temperature (351–371 K) for the β→λ phase transition. In addition, the pressure for the λ→β phase transition was further decreased to 35–40 MPa by compression on the (001) crystal plane, enabling it to have the promising capability for industrial thermal energy recovery, storage, and even for future lunar exploration applications.

Results

Sub-minute synthesis of β-Ti_3O_5 and λ-$M_xTi_{3-x}O_5$

The schematic illustration of the proposed LVS process is shown in Fig. 1a. This method differs from the traditional thermal reduction

[1]School of Materials Science and Engineering, Shanghai University, Shanghai, China. [2]State Key Laboratory of Advanced Special Steel, Shanghai University, Shanghai, China. [3]Key Laboratory of Interfacial Physics and Technology, Shanghai Institute of Applied Physics, Chinese Academy of Sciences, Shanghai, China. [4]Multidiscipline Research Center, Institute of High Energy Physics, Chinese Academy of Sciences, Beijing, China. [5]These authors contributed equally: Pengfei Zhao, Guangshi Li. ✉e-mail: guangshili@shu.edu.cn; xiongxiaolu@sinap.ac.cn; xlzou@shu.edu.cn; luxg@shu.edu.cn

process and enables the sub-minute synthesis of Ti_3O_5 from TiO_2[15–26]. Theoretically, the molten TiO_2 can be spontaneously decomposed to titanium suboxide and oxygen under vacuum conditions at a high temperature (Supplementary Fig. 1)[27,28]. Therefore, the single-phase of Ti_3O_5 can be obtained by precisely controlling the vacuum level and the temperature of the molten TiO_2 (Supplementary Fig. 2). With the assistance of laser, TiO_2 undergoes a high-temperature melt in a vacuum environment, leading to the fracture and recombination of Ti-O bonds (Supplementary Fig. 3). The composition of deoxygenation products of the TiO_2 melt is directly affected by the input power and the irradiation time of the laser (Supplementary Figs. 4 and 5). A single-phase of β-Ti_3O_5 can be facilely obtained under vacuum conditions of 10^{-3} Pa after irradiating TiO_2 with an 800 W laser for 60 s, followed by cooling to room temperature.

The X-ray diffraction (XRD) Rietveld refinement results suggested that the obtained β-Ti_3O_5 had a monoclinic crystal structure (space group: C2/m) with the lattice parameters $a = 9.747$ Å, $b = 3.801$ Å, and $c = 9.442$ Å (Fig. 1b and Supplementary Table 1). As shown in Fig. 1c, curve fitting was performed on the peaks of the Ti-2*p* XPS spectrum. Two peaks with binding energies of 464.6 and 458.8 eV were assigned to the characteristic Ti-$2p_{1/2}$ and Ti-$2p_{3/2}$, respectively. The Ti-$2p_{1/2}$ peak was well-fitted by two peaks centered at 464.8 eV and 463.9 eV, corresponding to the chemical states of Ti^{4+} and Ti^{3+}, respectively. For Ti-$2p_{3/2}$, two peaks centered at 458.9 eV and 458.4 eV were attributed to the two chemical states of Ti^{4+} and Ti^{3+}, respectively. The atomic structures of the synthesized β-Ti_3O_5 were further determined using high-angle annular dark-field scanning transmission electron microscopy (HAADF-STEM). Figure 1d shows a typical atomic-resolution HAADF-STEM image of the sample along the [010] zone axis where the bright spots represent the Ti atom columns that are consistent with the atomic configuration of β-Ti_3O_5. The typical interplanar distance (0.310 nm) combined with the fast Fourier transform result of the electron diffraction pattern was indexed to the (003) plane of the β-Ti_3O_5 crystalline phase, and this was consistent with the XRD pattern (PDF card No. 82-1138) (Supplementary Fig. 6). Furthermore, the in situ high-temperature X-ray diffraction (HTXRD) analysis displayed the evolution of the characteristic diffraction peaks, such as of λ-(20-3), λ-(203), and β-(20-3), β-(003), as they varied with temperature (Fig. 1e). Specifically, as the temperature increased, the β-phase underwent a phase transition to the λ phase (>453 K). Subsequently, at 473 K, it further transitioned to the α phase. Upon cooling, it returned to the λ phase (<473 K) and then recovered to the β-phase (<433 K) until

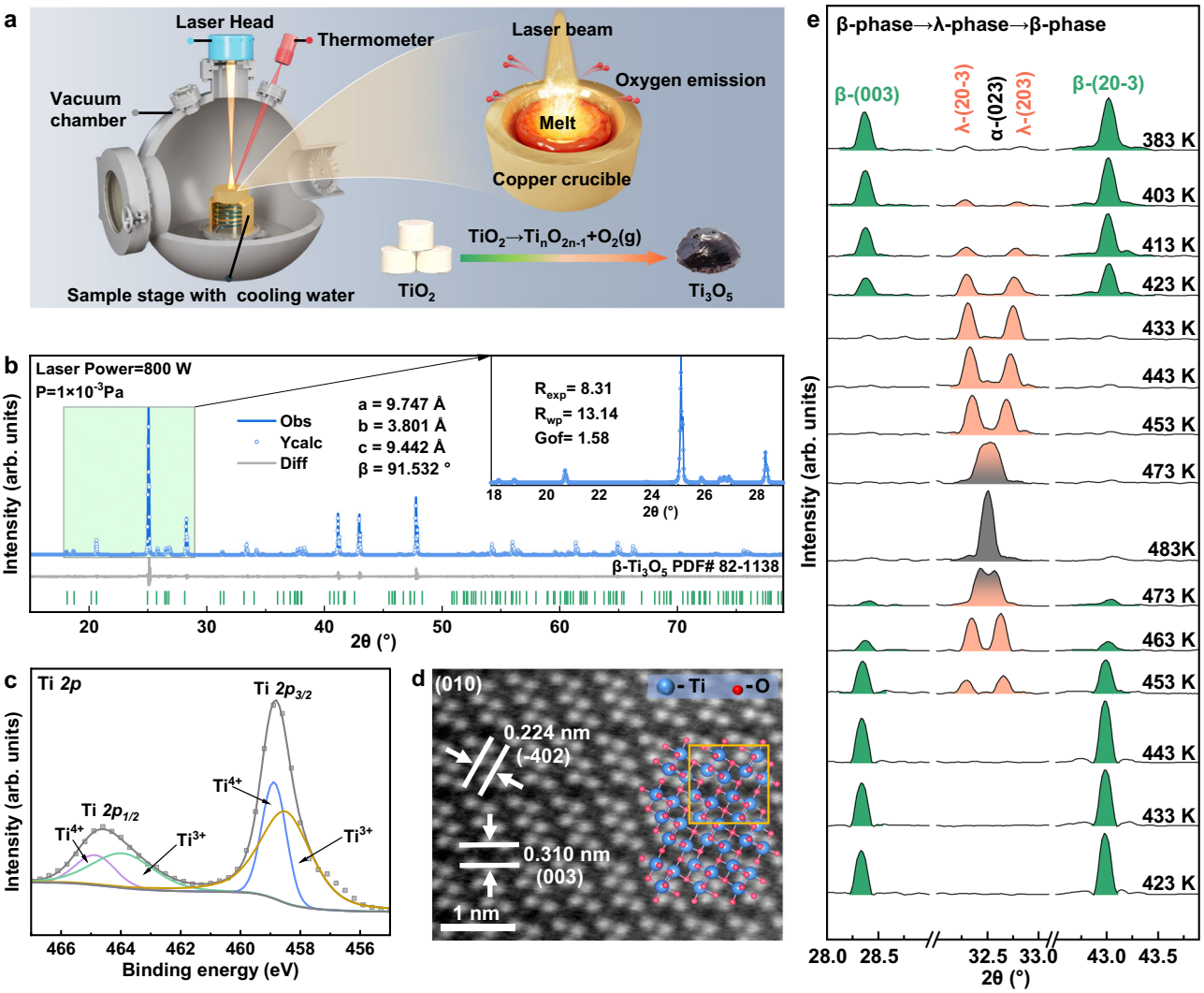

Fig. 1 | Synthesis, crystal structure, and phase transition properties of β-Ti_3O_5. **a** The experimental flow diagram for the synthesis of β-Ti_3O_5 using the laser-assisted vacuum smelting (LVS) method. **b** X-ray diffraction (XRD) Rietveld refinement result of β-Ti_3O_5 synthesized at 800 W for 60 s. Source data are provided as a Source Data file. **c** High-resolution X-ray photoelectron spectroscopy (XPS) spectra of the Ti 2*p* energy level from β-Ti_3O_5. **d** HAADF-STEM images of the as-synthesized β-Ti_3O_5. The inset shows the atomic structure model corresponding to the HAADF-STEM image, and the brightest columns in the image represent Ti atoms. **e** In situ HTXRD patterns of the as prepared β-Ti_3O_5 with a heating and cooling rate of 5 K/min.

reaching room temperature, demonstrating the reversible phase transition of β-Ti_3O_5 during the heating and cooling processes (Supplementary Fig. 7)[29–31]. Therefore, the β-Ti_3O_5 single phase synthesized from TiO_2 using the LVS method existed in the λ phase in the temperature range of 453 K to 473 K. Additionally, the DSC results reveal a distinct peak during both heating and cooling processes, corresponding to the reversible phase transition between β and λ phases (Supplementary Fig. 8). Specifically, the phase transition temperature from β to λ phase is 462 K, while the phase transition temperature from λ to β phase is 440 K, with corresponding phase transition enthalpies of 52.59 J/g (11.76 kJ/mol) and 52.01 J/g (11.63 kJ/mol), respectively.

β-Ti_3O_5 has been successfully synthesized using the LVS method; however, the λ-Ti_3O_5 phase was metastable at room temperature. To stabilize the λ-Ti_3O_5 at room temperature, ion substitution of λ-Ti_3O_5 has been shown to be a promising method[13,14,32–37]. Figure 2a shows two routes to obtain λ-$M_xTi_{3-x}O_5$ by the LVS method, i.e., (I) λ-$M_xTi_{3-x}O_5$ (M = Al or Sc) were obtained by directly adding Al_2O_3 or Sc_2O_3 to TiO_2, followed by laser-assisted vacuum decomposition. The parameters of laser power and irradiation time were 800 W and 60 s, respectively (Supplementary Figs. 9 and 10); and (II) λ-$M_xTi_{3-x}O_5$ (M = Mg, Al, Sc, V, Cr, Mn, or Fe) were obtained by adding MgO, Al_2O_3, Sc_2O_3, V_2O_3, Cr_2O_3, MnO, or FeO to β-Ti_3O_5, followed by laser-assisted melting. The parameters of laser power and irradiation time were 200 W and 20 s, respectively (Supplementary Fig. 11). A series of room-temperature stable λ-$M_xTi_{3-x}O_5$ (M = Mg, Al, Sc, V, Cr, Mn, or Fe, $0.09 \le x \le 0.42$) were successfully synthesized using the LVS method by mixing metal oxides (MgO, Al_2O_3, Sc_2O_3, V_2O_3, Cr_2O_3, MnO, or FeO) and TiO_2 as raw materials. (Supplementary Figs. 12–25). Note that when mixing other metal oxides (including SiO_2, CaO, CoO, NiO, CuO, or ZnO), λ-$M_xTi_{3-x}O_5$ (M = Si, Ca, Co, Ni, Cu, or Zn, $x = 0.15$) could not be obtained using the above two routes (Supplementary Fig. 26).

To evaluate the phase transition process of λ-$M_xTi_{3-x}O_5$ (M = Mg, Al, Sc, V, Cr, Mn, or Fe) from λ to β, DFT calculations were employed to study the phase transition mechanism (Supplementary Table 2). Different substitution sites involving Ti1, Ti2, and Ti3 for all λ-$M_xTi_{3-x}O_5$ materials were studied (Supplementary Figs. 27 and 28). The results indicate that compared with Ti1 and Ti2 site substitutions, the Ti3 site substitution shows more negative total energies, indicating that Ti3 substitution leads to more stable configurations (Supplementary Tables 3 and 4). As shown in Fig. 2b and Supplementary Figs. 29–36, a series of transition processes from λ-$M_xTi_{3-x}O_5$ to β-$M_xTi_{3-x}O_5$ were investigated. All λ-$M_xTi_{3-x}O_5$ structures adapted in the calculations are consistent with the doping ratios observed in the experiments, while also considering Ti3 site substitution. λ-Ti_3O_5 transformed to β-Ti_3O_5 via breaking of the Ti3–O5 bond and formation of the Ti3–O4 bond with a transition energy barrier of 1.22 eV, which was similar to the phase transition mechanism from β-Ti_3O_5 to λ-Ti_3O_5 revealed by Liu et al.[38]. The results showed that the metal substitution led to an increase in the transition energy barriers compared with Ti_3O_5. In addition, the λ-$M_xTi_{3-x}O_5$ phase was more favored energetically than β-$M_xTi_{3-x}O_5$, indicating greater stability of λ-$M_xTi_{3-x}O_5$. The transition from λ-Ti_3O_5 to β-Ti_3O_5 was spontaneous as the temperature decreased. Therefore, the transition from λ-$M_xTi_{3-x}O_5$ to the β-$M_xTi_{3-x}O_5$ phase required an external driving force, such as pressure. Evidently, λ-$Al_xTi_{3-x}O_5$ required the lowest energy barrier, indicating that the transition from λ-$Al_xTi_{3-x}O_5$ to β-$Al_xTi_{3-x}O_5$ was achieved more easily, i.e., the required pressure was the lowest. Subsequently, the transition process from λ-$Al_xTi_{3-x}O_5$ to β-$Al_xTi_{3-x}O_5$ was performed based on a supercell of $1 \times 1 \times 2$ that included two Ti3–Ti3 layers (Fig. 2c). The energy barriers for transition from the λλ-phase to the λβ-phase and the λβ-phase to the ββ-phase were 2.21 eV and 1.77 eV, respectively. This result indicated that the energy barrier decreased once the transition occurred. The computational results indicated that the phase transition process from λ-$M_xTi_{3-x}O_5$ to β-$M_xTi_{3-x}O_5$ was achieved by the movements of the Ti3–Ti3 dimers and the corresponding oxygen atoms, while the Ti1 and Ti2 atoms remained nearly unchanged. Additionally, once a phase transition is initiated within a single unit cell, subsequent transitions proceed with a lower energy barrier, thereby facilitating the transition from λ-$M_xTi_{3-x}O_5$ to β-$M_xTi_{3-x}O_5$.

Pressure-temperature induced phase transition of λ-$M_xTi_{3-x}O_5$

To further explore the structure and phase transition properties of λ-$Al_xTi_{3-x}O_5$, in situ and ex situ XRD characterizations were conducted. As shown in Fig. 3a, λ-$Al_{0.12}Ti_{2.88}O_5$ possessed a monoclinic structure (space group: C2/m), with lattice parameters $a = 9.802$ Å, $b = 3.777$ Å, and $c = 9.951$ Å (Supplementary Fig. 37). The transmission electron microscopy (TEM) image shows irregular block particles of λ-$Al_{0.12}Ti_{2.88}O_5$ (Supplementary Fig. 38). The HAADF-STEM image and atomic-scale energy dispersive X-ray spectroscopy (EDS) mappings confirmed that Al replaced Ti atoms into the β-Ti_3O_5 lattice (Fig. 3b and Supplementary Fig. 39). The high-resolution HAADF-STEM images of λ-$Al_{0.12}Ti_{2.88}O_5$ along the [010] zone axis, as shown in Fig. 3c and Supplementary Fig. 40, were consistent with the atomical configuration. The typical interplanar distances of 0.509 nm and 0.521 nm corresponded to the (200) and (002) planes in the monoclinic structure, respectively, in agreement with the XRD pattern (PDF card no. 82-1137).

The high-pressure XRD measurements results revealed that as the applied pressure increased, the intensity of the diffraction peaks corresponding to λ-(20-3) and λ-(203) gradually diminished, while the diffraction peaks associated with β-(20-3) and β-(003) gradually intensified, suggesting a gradual phase transition from the λ to the β-phase (Fig. 3d and Supplementary Figs. 41 and 42). The cross-pressure for the phase transition of λ-$Al_{0.12}Ti_{2.88}O_5$ was estimated to be approximately 557 MPa (Supplementary Fig. 43). The similar phase transition from the λ to the β-phase was also observed in λ-$M_xTi_{3-x}O_5$ (M = Mg, Sc, V, Cr, Mn, or Fe) (Supplementary Figs. 44–50). Figure 3e and Supplementary Fig. 51 show that as the temperature increased from 300 K (25 °C) to 363 K (90 °C), the diffraction peaks of β-(20-3) and β-(003) gradually weakened, while the diffraction peaks of λ-(20-3) and λ-(203) gradually strengthened. This result indicated the gradual transition of the β-phase into the λ-phase with an estimated crossover temperature of ~363 K (Supplementary Fig. 52). Upon further heating to 403 K, the diffraction peaks for the β-phase nearly vanished, indicating the transition from the β-phase to the λ-phase was completed. At high temperatures (>453 K), the λ-phase undergoes a second-order phase transition to the α phase, but then it reverts to the λ-phase upon cooling. Therefore, during the cooling process, the α-phase underwent a phase transition to the λ phase that existed stably in the temperature range of 403–300 K. A similar phase transition from β-phase to λ-phase was also observed in β-$M_xTi_{3-x}O_5$ (M = Mg, Sc, V, Cr, Mn, or Fe) (Supplementary Figs. 53–57). Furthermore, the enthalpy during the β→λ phase transition directly reflected the heat storage capacity of β-$M_xTi_{3-x}O_5$. The differential scanning calorimetry test results showed that, except for β-$Mn_xTi_{3-x}O_5$, the above pressure-treated samples exhibited significant endothermic peaks, with β-$Al_xTi_{3-x}O_5$ having more pronounced heat storage capabilities (Fig. 3f and Supplementary Fig. 58). When x decreased from 0.13 to 0.10, the phase transition enthalpy of β-$Al_xTi_{3-x}O_5$ increased from 15.70 J/g (3.51 kJ/mol) to 21.78 J/g (4.87 kJ/mol), and the phase transition temperature increased from 351 K to 371 K. It is noted that β-$Al_xTi_{3-x}O_5$ had an excellent heat storage performance, showing reversible phase transition characteristics under the influence of external pressure and temperature. However, the phase transition pressure from λ to β still required several hundred MPa, making the application limited.

To understand the phase transition and develop a new strategy to further reduce the phase transition pressure of λ-$Al_{0.12}Ti_{2.88}O_5$, the microstructure of λ-$Al_{0.12}Ti_{2.88}O_5$ after pressure treatment was investigated. The sample showed distinct phase interfaces between the β and λ phases (Supplementary Fig. 59). Further analysis at the interfaces showed that the β and λ grains had a specific orientation relationship of

https://doi.org/10.1038/s41467-025-57604-0

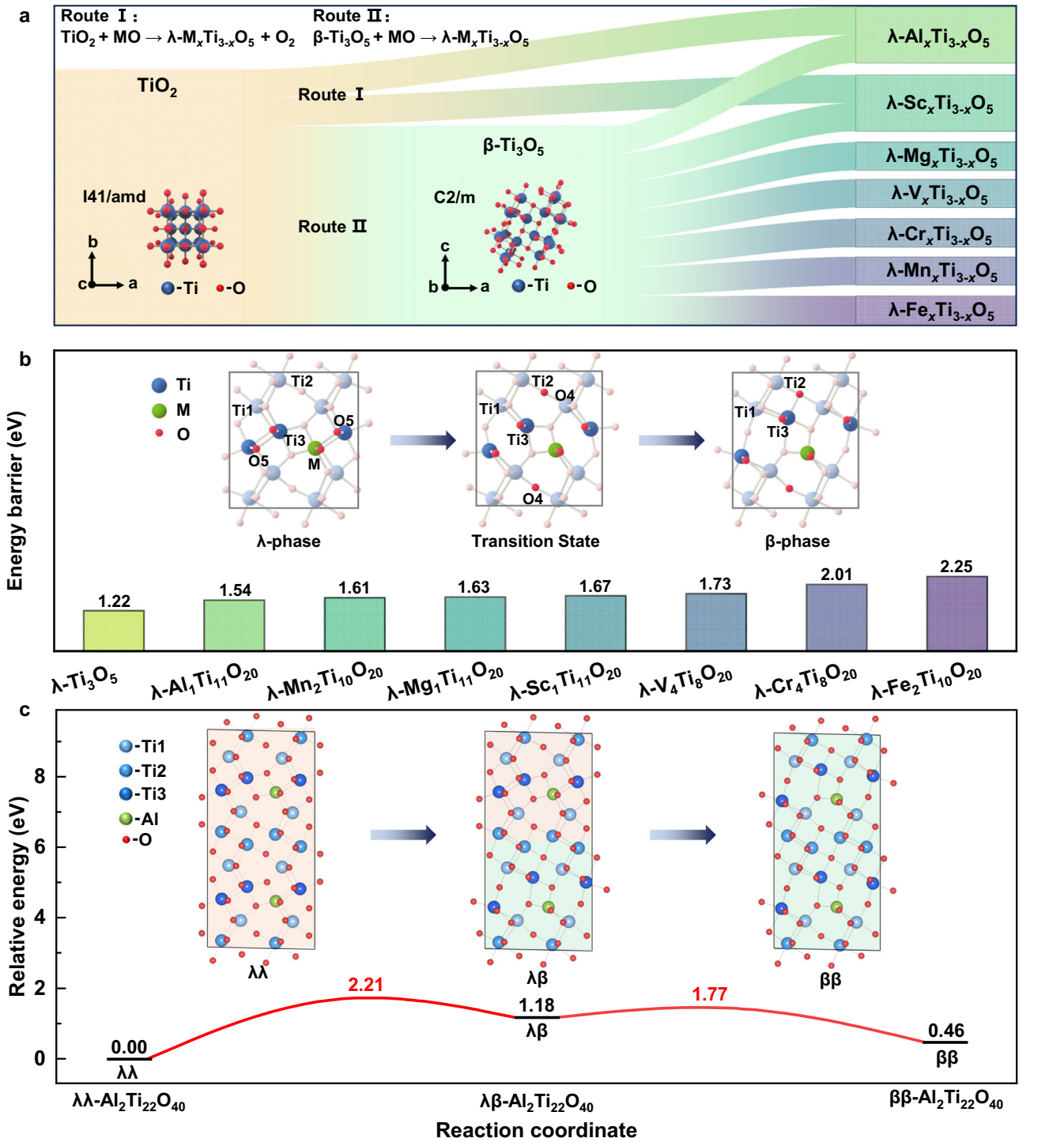

Fig. 2 | Synthesis routes of λ-$M_xTi_{3-x}O_5$ and the phase transition mechanism from the λ to the β phase. a The routes for synthesizing room temperature stable λ-$M_xTi_{3-x}O_5$ with different metal substitutions: Route I: laser-assisted vacuum decomposition, TiO_2 + MO → λ-$M_xTi_{3-x}O_5$ + O_2 (M = Al or Sc); Route II: laser-assisted melting, β-Ti_3O_5 + MO → λ-$M_xTi_{3-x}O_5$ (M = Al, Sc, Mg, V, Cr, Mn, or Fe). The insets are the structures of anatase-TiO_2 and β-Ti_3O_5. **b** The energy barriers for the transition from the λ-phase to the β-phase using the density functional theory (DFT) calculations. The insets are the structures of the λ-phase, the transition state, and the β-phase. **c** The energy barriers for the transition from the λλ-phase to the ββ-phase of λ-$Al_xTi_{3-x}O_5$ using the density functional theory (DFT) calculations. The insets are the structures of λ-$Al_xTi_{3-x}O_5$, the λβ stacking metastable phase, and β-$Al_xTi_{3-x}O_5$.

$[010]_β$//$[010]_λ$, $[001]_β$//$[001]_λ$, and $(100)_β$//$(100)_λ$, respectively (Fig. 3g), indicating a high degree of lattice matching between β- and λ-$Al_{0.12}Ti_{2.88}O_5$ (Fig. 3h). The close-up integrated differential phase contrast (iDPC)-STEM images revealed the atomic stacking order at the phase interface along the [010] zone axis (Fig. 3i and Supplementary Fig. 60). To achieve atomic-scale matching, Ti atoms were stacked in the sequence of ···Ti2-Ti1-Ti3-Ti3-Ti1-Ti2··· along the [001] zone axis, and the β as well as λ phases were interconnected through the $Ti2_β$ and $Ti2_λ$ layer. Based on the DFT calculation results and the unique structural configuration observed at the phase interface, it was inferred that compression on the (001) crystal plane of the λ phase may be an effective pathway to greatly reduce the excessively high pressure for its transition to the β-phase.

https://doi.org/10.1038/s41467-025-57604-0

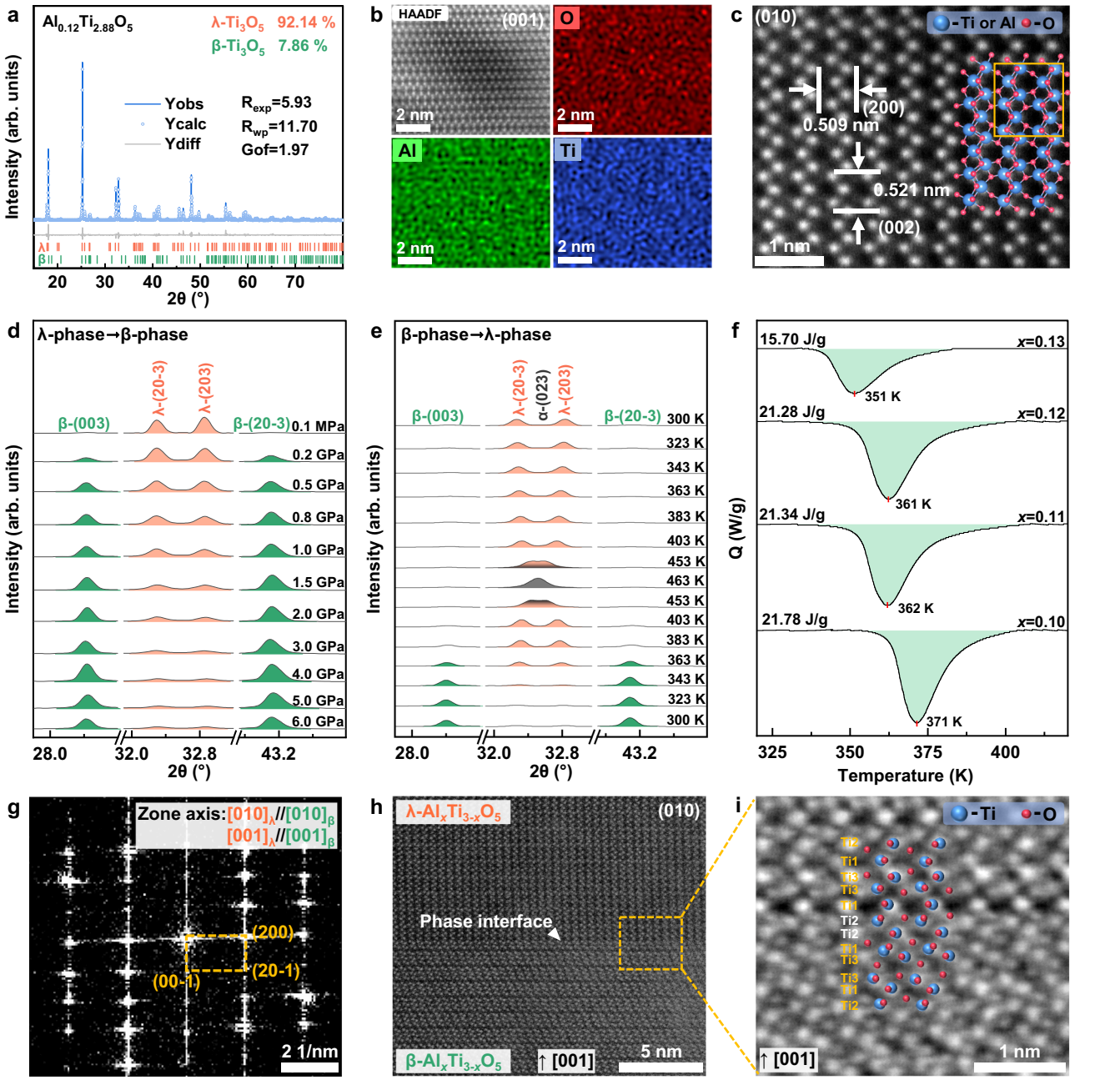

Fig. 3 | Crystal structure and the reversible phase transition properties of λ-$Al_{0.12}Ti_{2.88}O_5$. **a** The XRD Rietveld refinement result of the as-synthesized λ-$Al_{0.12}Ti_{2.88}O_5$ (λ phase: PDF card No. 82-1137; β phase: PDF card No. 82-1138). Source data are provided as a Source Data file. **b** The HAADF-STEM image and electron energy loss spectroscopy atomic mapping of the as-prepared λ-$Al_{0.12}Ti_{2.88}O_5$. **c** High-resolution HAADF-STEM image of the λ-$Al_{0.12}Ti_{2.88}O_5$ phase along the [010] zone axes. The inset displays the atomic structure model corresponding to the HAADF-STEM image, and the brightest columns in the image represent the Ti or Al atoms. **d** XRD patterns of λ-$Al_{0.12}Ti_{2.88}O_5$ in the range of 0.2 MPa to 6 GPa. **e** HTXRD patterns of β-$Al_{0.12}Ti_{2.88}O_5$ in the range of 300 K and 463 K. **f** Differential scanning calorimetry curves of the β-$Al_xTi_{3-x}O_5$ ($x = 0.10$, 0.11, 0.12 and 0.13). **g** Fast Fourier transform of Supplementary Fig. 59 at the interface shows that the β and λ grains have a specific orientation relationship of $[010]_β//[010]_λ$, $[001]_β//[001]$, and $(100)_β//(100)_λ$. **h** HAADF-STEM image of an β/λ-$Al_{0.12}Ti_{2.88}O_5$ phase interface taken from the post-compression λ-$Al_{0.12}Ti_{2.88}O_5$ along the [010] zone axes. **i** The close-up integrated differential phase contrast (iDPC)-STEM image revealed the atomic stacking order at the phase interface in the region highlighted by the orange dashed square in (**h**).

Accordingly, to investigate the phase transition characteristics along the [001] zone axis of the λ-$Al_{0.12}Ti_{2.88}O_5$, we conducted uniaxial static compression tests for micropillars. A crystal grain with (001) preferred orientation was identified in λ-$Al_{0.12}Ti_{2.88}O_5$ using an electron backscatter diffraction orientation analysis. Next, we utilized a top-down focused-ion beam fabrication procedure to obtain the [001]-oriented micropillars to study the stress-strain behavior of λ-$Al_{0.12}Ti_{2.88}O_5$ (Fig. 4a and Supplementary Fig. 61). In the uniaxial static compression tests, significant strain was detected in the cylindrical micropillars (Supplementary Movies 1 and 2), but no cracking phenomenon was observed in the micropillar 2 (Fig. 4b, c). The stress–strain curve demonstrated that the occurrence of significant plastic deformation was found in the cylindrical micropillars during the compression process (Supplementary Figs. 62 and 63). Figure 4d shows that the micropillar underwent typical elastic deformation during the initial stage (stage I). When the pressure reached 35–40 MPa, significant plastic deformation occurred (stage II) that resulted in a phase transition from the λ-phase to the β-phase.

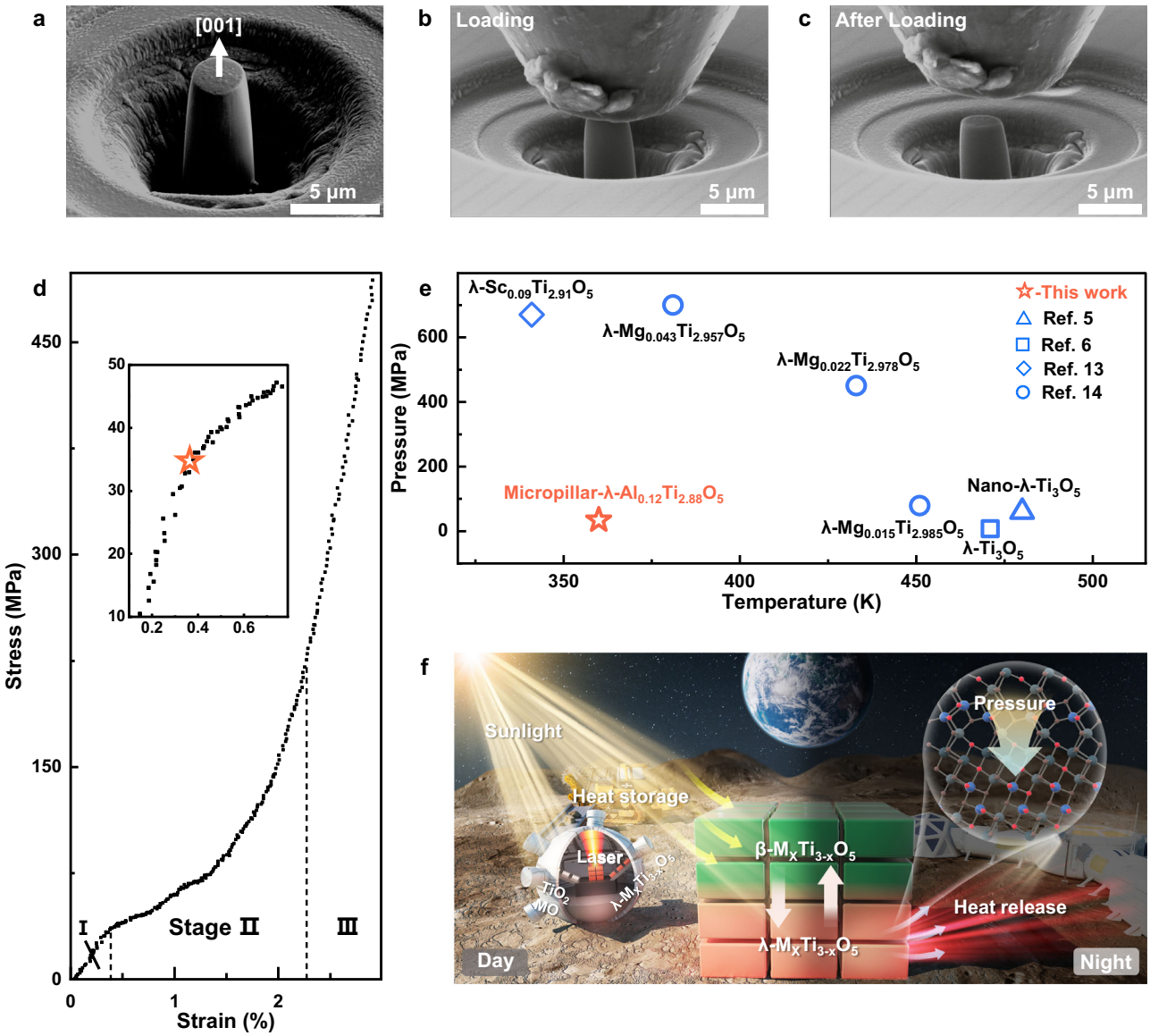

Fig. 4 | The [001] uniaxial static compression experiment. a [001]-oriented λ-$Al_{0.12}Ti_{2.88}O_5$ micropillar 2 with a height-to-diameter ratio of 2:1. **b**, **c** Scanning electron microscopy images of micropillar 2 during and after loading, captured in the in-situ test. The compression tests were conducted using an Alemnis Standard Assembly platform that was equipped with a diamond flat punch indenter with a diameter of 10 μm. **d** The obtained stress-strain curve during the in-situ compression process; Stage I: Typical elastic deformation during the initial stage; Stage II: Plastic deformation occurred, resulting in a phase transition from the λ-phase to the β-phase; Stage III: The material reverted back to elastic deformation. The orange stars represent the phase transition pressure of micropillar 2. Source data are provided as a Source Data file. **e** Comparisons of this work with the reported results in terms of the phase transition temperature and pressure. **f** Schematic representation of the possible heat storage system with β/λ-$Al_xTi_{3-x}O_5$ as the fundamental material for future lunar explorations.

After the pressure exceeded 200 MPa, the material reverted back to the elastic deformation (stage III). During the unloading, the strain of the micropillar partially recovered. We further analyzed the microstructure of the post-compression micropillar 2. A typical atomic structure of the β-phase was observed, indicating a phase transition from the λ-phase to the β-phase after compression (Supplementary Fig. 64b–d). These findings further confirmed that applying pressure on the (001) crystal plane was an effective approach to fundamentally address the issue of excessive pressure during the λ→β phase transition.

Discussion

A series of ceramics, namely λ-$M_xTi_{3-x}O_5$ (M = Mg, Al, Sc, V, Cr, Mn, or Fe), were synthesized using the LVS method. The LVS method has demonstrated many advantages such as sub-minute reaction times (20–60 s), reductant-free, and feasible synthesis routes (Supplementary Table 5). The ceramic, λ-$Al_xTi_{3-x}O_5$, exhibited a more pronounced heat storage performance (15.70 J/g–21.78 J/g) with a phase transition temperature range of 351–371 K. However, the phase transition pressure of λ-$M_xTi_{3-x}O_5$ needs to exceed several hundred MPa, such as λ-$Al_{0.12}Ti_{2.88}O_5$ (557 MPa) and λ-$Sc_{0.09}Ti_{2.91}O_5$ (680 MPa)[13], and this poses a significant challenge for practical applications. The primary external factor that triggers the transition from λ-$M_xTi_{3-x}O_5$ to β-$M_xTi_{3-x}O_5$ is compression on the (001) crystal plane (c-axis) of λ-phase. In polycrystalline powders, λ-$M_xTi_{3-x}O_5$ grains typically exhibit anisotropy, whereby compression, the actual stresses on the (001) crystal plane are insufficient to induce the λ → β phase transition[39,40]. Therefore, we proposed a strategy of applying pressure along the [001] zone axis of λ-$Al_xTi_{3-x}O_5$ to investigate the process of pressure-induced phase transition on the (001) crystal plane. In uniaxial static compression

experiments, the λ→β phase transition was induced at an extremely low pressure (approximately 35–40 MPa), which was more than ten times lower than polycrystalline powders (Fig. 4e). In addition, as the proposed laser-based synthesis method utilizes vacuum metallurgy, it holds potential for future applications in vacuum environments, such as applications for future lunar thermal energy management. With lunar surface solar radiation as the heat source and lunar regolith[41,42] (rich in Ti and Al elements) as the raw material[43,44], there is potential for the in-situ preparation and utilization of λ-$M_xTi_{3-x}O_5$ ceramics for thermal storage applications (Fig. 4f).

In summary, the proposed LVS method and uniaxial compression strategy were shown to substantially enhance the synthesis efficiency and minimize the phase transition pressure. Therefore, achieving reversible phase transitions between the λ and β phases at low pressures (35–40 MPa) and temperatures (363 K) in λ-$Al_xTi_{3-x}O_5$ heat storage ceramics has become feasible with a pressure well below the recently reported 680 MPa. This work presented a proof-of-concept for further reducing the phase transition pressure of λ-Ti_3O_5-based ceramics and provided a method for the synthesis and modulation of λ-$M_xTi_{3-x}O_5$ ceramics for potential wide applications in thermal energy management. The principles of element substitution and crystal plane modulation may also be applicable to other pressure-induced heat-storage materials.

Methods

Chemicals

TiO_2 (≥98.00%), MgO (98.50%), Al_2O_3 (99.99%), SiO_2(99.90%), CaO (97.00%), Sc_2O_3 (99.90%), V_2O_3 (95.00%), Cr_2O_3(99.00%), MnO (99.00%), FeO (99.50%), CoO (99.00%), NiO (98.00%), CuO (99.50%), ZnO (99.00%) were purchased from Sinopharm Chemical Reagent Co., Ltd.

Material synthesis by laser-assisted vacuum smelting (LVS)

Our experiments were carried out in a vacuum thermal decomposition system with a pressure better than 1×10^{-3} Pa. β-Ti_3O_5 and λ-$M_xTi_{3-x}O_5$ were synthesized using the LVS method. In this method, TiO_2 powder or a mixture powder (metal oxides and TiO_2 powder were homogeneously mixed) was pressed into tablets with a diameter of 7 mm under a uniaxial pressure of 100 MPa and placed into a copper crucible. The crucible was then transferred to a vacuum cavity and decomposed at different powers and times under a pressure of 1×10^{-3} Pa. Subsequently, the synthesized products were ground into fine powders for further characterization.

X-ray diffraction measurement

The crystal structures of β-Ti_3O_5 and λ-$M_xTi_{3-x}O_5$ were determined by X-ray diffraction instrument (XRD, Bruker D8 ADVANCE A25X, Germany) using Cu-Kα radiation with a scan rate of 1° min^{-1}. The In-situ HTXRD measurements were carried out using an Anton Paar XRK 900 reaction chamber with a heating rate of 5 K/min and a holding time of 5 min at each temperature interval (λ = 1.5406 Å). The phase components were calculated by Rietveld refinement analysis using Total Pattern Analysis Solutions (TOPAS) 4.2 software.

Theoretical calculations

All calculations were performed using Vienna ab-initio Simulation Package (VASP). The projector-augmented wave method was used[45,46]. The exchange-correlation energy was described by generalized gradient approximation (GGA), employing the Perdew–Burke–Ernzerhof functional[47]. The calculations were optimized with an energy cutoff of 520 eV and the convergence criteria for force and energy are set to 0.01 eV/Å and 10^{-6} eV, respectively. For Brillouin zone integration[48], the k-point mesh was set to 3 × 3 × 3. As shown in Supplementary Fig. 27, the crystalline structure for λ-Ti_3O_5 and β-Ti_3O_5 is the monoclinic and C2/m crystal, consisting of 12 Ti and 20 O atoms. As listed in Supplementary Table 2, the calculated lattice parameters of both λ- and β-Ti_3O_5 are consistent with the experimental results[5]. After optimization, according to the realistic ratio in the experiment, different contents of Mg, Al, Sc, V, Cr, Mn or Fe were used to replace the Ti atoms in λ-$Ti_{12}O_{20}$, resulting in λ-$Mg_1Ti_{11}O_{20}$, λ-$Al_1Ti_{11}O_{20}$, λ-$Sc_1Ti_{11}O_{20}$, λ-$V_2Ti_{10}O_{20}$, λ-$Cr_4Ti_8O_{20}$, λ-$Mn_4Ti_8O_{20}$, and λ-$Fe_2Ti_{10}O_{20}$. In addition, a 1 × 1 × 2 supercell containing 64 atoms of λ-$Al_2Ti_{22}O_{40}$ was employed to investigate the transformation from the λλ-phase to the ββ-phase. All transition state structures were located by using the climbing image nudged elastic band (CI-NEB) methods[49]. All calculations were spin-polarized.

Static compression testing

λ-$M_xTi_{3-x}O_5$ powder was molded into cylinders (Φ 3.0 × 3.0 mm^2) and loaded into a high-pressure device (ZSM-10G, Zhengzhou Abrasives Grinding Institute, China). Then, the samples were pressed at different pressures. The pressure was calibrated by Bi and ZnTe phase transitions at high pressures.

High-pressure synchrotron XRD experiments

In situ high-pressure X-ray diffraction experiments were carried out at the 4W2 beamline of the Beijing Synchrotron Radiation Facility using a wavelength of 0.6199 Å. A symmetric diamond anvil cell with a 300 μm culet size was used for the measurements. The prepared λ-$M_xTi_{3-x}O_5$ was placed into a 130 μm diameter hole in a pre-indented Re gasket with a thickness of 40 μm for XRD. The pressures were calibrated according to the ruby fluorescence method with an error of ±0.1 GPa[50]. The powder diffraction patterns were collected by a Pilatus 3 × 2 M image plate and integrated using the FIT2D software package.

X-ray photoelectron spectroscopy

X-ray photoelectron spectroscopy (XPS) analysis was conducted on a Thermal SCIENTIFIC ESCALAB 250XI system with a base pressure of ~2×10^{-9} mbar. The spectra were obtained using an Al K_α radiation ($h\upsilon$ = 1486.6 eV) beam (500 μm, 25 W). Binding energy was calibrated by the adventitious C 1s peak at 284.8 eV.

Thermal property measurement

The heat absorption properties of λ-$M_xTi_{3-x}O_5$ were measured by differential scanning calorimetry (DSC, PerkinElmer STA-8000) with a heating/cooling rate of 5 K/min and an air gas flow of 100 mL/min. Before testing, all samples were compressed by 6 GPa static high pressure to change their phase composition from λ phase to β phase.

TEM and HRTEM observations

The atomic structures of the synthesized β-Ti_3O_5 and λ-$Al_xTi_{3-x}O_5$ were characterized in Hitachi HF5000 under a voltage of 200 kV and atomic-resolution high-angle annular dark-field scanning transmission electron microscopy (HAADF-STEM) images were obtained. The cross-sectional microstructures perpendicular to the pressure were characterized in FEI Titan Cubed Themis G2 300 under a voltage of 300 kV. The HAADF-STEM and iDPC images of the phase interface in β/λ-$Al_xTi_{3-x}O_5$ were obtained. Atomic-resolution Annular dark field (ADF-STEM) images of the cross-sectional microstructures in cylindrical micropillars were obtained, using a double aberration-corrected JEOL JEM-ARM 300 under a voltage of 300 kV.

Micromechanical testing

Cylindrical micropillars with a height-to-diameter ratio of 2:1 were prepared along the [001]-oriented using focused-ion beam (FIB) milling technique (Helios G4 PFIB, Thermo Fisher, USA). In-situ compression tests were conducted using an Alemnis Standard Assembly platform, which was equipped with a diamond flat punch indenter with a diameter of 10 μm.

Data availability

The data generated in this study are provided in the Supplementary Information/Source Data file. Source data are provided with this paper.

References

1. Forman, C., Muritala, I. K., Pardemann, R. & Meyer, B. Estimating the global waste heat potential. *Renew. Sustain. Energy Rev.* **57**, 1568–1579 (2016).
2. Zhang, Z. et al. Thermal batteries based on inverse barocaloric effects. *Sci. Adv.* **9**, eadd0374 (2023).
3. Ohkoshi, S. et al. Synthesis of a metal oxide with a room-temperature photoreversible phase transition. *Nat. Chem.* **2**, 539–545 (2010).
4. Yang, B. et al. Flatband λ-Ti_3O_5 towards extraordinary solar steam generation. *Nature* **622**, 499–506 (2023).
5. Tokoro, H. et al. External stimulation-controllable heat-storage ceramics. *Nat. Commun.* **6**, 1–8 (2015).
6. Ohkoshi, S.-i. et al. Low-pressure-responsive heat-storage ceramics for automobiles. *Sci. Rep.* **9**, 13203 (2019).
7. Sato, H. et al. Baddeleyite-type high-pressure phase of TiO_2. *Science* **251**, 786–788 (1991).
8. Huang, L., Durandurdu, M. & Kieffer, J. Transformation pathways of silica under high pressure. *Nat. Mater.* **5**, 977–981 (2006).
9. Karzel, H. et al. Lattice dynamics and hyperfine interactions in ZnO and ZnSe at high external pressures. *Phys. Rev. B* **53**, 11425 (1996).
10. Chen, Y. et al. Pressure–temperature phase diagram of vanadium dioxide. *Nano Lett.* **17**, 2512–2516 (2017).
11. Arcangeletti, E. et al. Evidence of a pressure-induced metallization process in monoclinic VO_2. *Phys. Rev. Lett.* **98**, 196406 - (2007).
12. Hu, L. et al. Unveiling the mechanisms of metal-insulator transitions in V_2O_3: the role of trigonal distortion. *Phys. Rev. B* **103**, 085119 (2021).
13. Nakamura, Y., Sakai, Y., Azuma, M. & Ohkoshi, S. Long-term heat-storage ceramics absorbing thermal energy from hot water. *Sci. Adv.* **6**, eaaz5264 (2020).
14. Ohkoshi, S. et al. Pressure effect on long-term heat storage ceramics based on Mg-substituted λ-Ti_3O_5. *Mater. Adv.* **3**, 4824–4830 (2022).
15. Andersson, S., Collén, B., Kuylenstierna, U. & Magnéli, A. Phase analysis studies on the titanium-oxygen system. *Acta Chem. Scand.* **11**, 1641–1652 (1957).
16. Dring, K., Dashwood, R. & Inman, D. Voltammetry of titanium dioxide in molten calcium chloride at 900 °C. *J. Electrochem. Soc.* **152**, E104 (2005).
17. Kar, P. & Evans, J. W. Determination of kinetic parameters by modeling of voltammograms for electrochemical reduction of titanium dioxide. *Electrochem. Commun.* **8**, 1397–1403 (2006).
18. Kitada, A. et al. Selective preparation of macroporous monoliths of conductive titanium oxides Ti_nO_{2n-1} (n = 2, 3, 4, 6). *J. Am. Chem. Soc.* **134**, 10894–10898 (2012).
19. Chai, G., Huang, W., Shi, Q., Zheng, S. & Wei, D. Preparation and characterization of λ-Ti_3O_5 by carbothermal reduction of TiO_2. *J. Alloy. Compd.* **621**, 404–410 (2015).
20. Li, X. et al. The synthesis and gas sensitivity of the β-Ti_3O_5 powder: Experimental and DFT study. *J. Alloy. Compd.* **649**, 939–948 (2015).
21. Shi, Q. et al. Fabrication of nanocrystalline λ-Ti_3O_5 with tunable terahertz wave transmission properties across a temperature-induced phase transition. *J. Mater. Chem. C* **4**, 10279–10285 (2016).
22. Wang, L. et al. Electrochemical properties of Ti_3O_5 powders prepared by carbothermal reduction. *J. Mater. Sci. Mater. Electron* **28**, 6421–6425 (2017).
23. Cai, Y. et al. Synthesis of nanoscale lambda-Ti_3O_5 via a PEG-assisted sol-gel method. *J. Alloy. Compd.* **848**, 156585 (2020).
24. Mariette, C. et al. Strain wave pathway to semiconductor-to-metal transition revealed by time-resolved X-ray powder diffraction. *Nat. Commun.* **12**, 1239 (2021).
25. Yang, S. et al. A novel carbon thermal reduction approach to prepare recorded purity β-Ti_3O_5 compacts from titanium dioxide and phenolic resin. *J. Alloy. Compd.* **853**, 157360 (2021).
26. Fu, X. et al. Preparing high purity λ-Ti_3O_5 and Li/λ-Ti_3O_5 as high-performance electromagnetic wave absorbers. *J. Mater. Chem. C* **9**, 7976–7981 (2021).
27. Browne, R. J. A review of the fundamentals of vacuum metallurgy. *Vacuum* **21**, 13–16 (1971).
28. Xu, B., Sohn, H. Y., Mohassab, Y. & Lan, Y. Structures, preparation and applications of titanium suboxides. *RSC Adv.* **6**, 79706–79722 (2016).
29. Åsbrink, S. & Magnéli, A. Crystal structure studies on trititanium pentoxide, Ti_3O_5. *Acta Crystallogr* **12**, 575–581 (1959).
30. Rao, C., Ramdas, S., Loehman, R. & Honig, J. Semiconductor-metal transition in Ti_3O_5. *J. Solid State Chem.* **3**, 83–88 (1971).
31. Onoda, M. Phase transitions of Ti_3O_5. *J. Solid State Chem.* **136**, 67–73 (1998).
32. Grey, I. & Ward, J. An X-ray and Mössbauer study of the $FeTi_2O_5$-Ti_3O_5 system. *J. Solid State Chem.* **7**, 300–307 (1973).
33. Shen, Z. et al. Stabilization of microcrystal λ-Ti_3O_5 at room temperature by aluminum-ion doping. *Appl Phys. Lett.* **111**, 191902 (2017).
34. Wang, M. et al. Phase evolution and formation of λ phase in Ti_3O_5 induced by magnesium doping. *J. Alloy. Compd.* **774**, 1189–1194 (2019).
35. Takahama, R. et al. Structural, magnetic, transport, and thermoelectric properties of the pseudobrookite $AlTi_2O_5$–Ti_3O_5 system. *Phys. Rev. Mater.* **4**, 074401 (2020).
36. Ohkoshi, S., Yoshikiyo, M., MacDougall, J., Ikeda, Y. & Tokoro, H. Long-term heat-storage materials based on λ-Ti_3O_5 for green transformation (GX). *Chem. Commun.* **59**, 7875–7886 (2023).
37. Otake T. et al. Long-term heat-storage ceramics based on Zr-Substituted λ-Ti_3O_5. *Eur. J. Inorg. Chem.* **27**, e202400047 (2024).
38. Liu, M. et al. Layer-by-layer phase transformation in Ti_3O_5 revealed by machine-learning molecular dynamics simulations. *Nat. Commun.* **15**, 3079 (2024).
39. Jütten, S. & Bredow, T. Doping effect on the electronic structure and heat-storage properties of Ti_3O_5. *J. Phys. Chem. C.* **127**, 10445–10452 (2023).
40. Jütten, S. & Bredow, T. Anisotropy of the pressure effect in the Ti_3O_5 phase transition process resolved by direction-dependent interface propagation. *J. Phys. Chem. C.* **127**, 20530–20538 (2023).
41. Farries, K. W., Visintin, P., Smith, S. T. & van Eyk, P. Sintered or melted regolith for lunar construction: state-of-the-art review and future research directions. *Constr. Build Mater.* **296**, 123627 (2021).
42. Ross, B., Haussener, S. & Brinkert, K. Assessment of the technological viability of photoelectrochemical devices for oxygen and fuel production on Moon and Mars. *Nat. Commun.* **14**, 3141 (2023).
43. Yao, Y., Xiao, C., Wang, P., Li, C. & Zhou, Q. Instrumental neutron activation analysis of Chang'E-5 lunar regolith samples. *J. Am. Chem. Soc.* **144**, 5478–5484 (2022).
44. Che, X. et al. Age and composition of young basalts on the Moon, measured from samples returned by Chang'e-5. *Science* **374**, 887–890 (2021).
45. Kresse, G. & Furthmüller, J. Efficient iterative schemes for ab initio total-energy calculations using a plane-wave basis set. *Phys. Rev. B* **54**, 11169 (1996).
46. Kresse, G. & Furthmüller, J. Efficiency of ab-initio total energy calculations for metals and semiconductors using a plane-wave basis set. *Comp. Mater. Sci.* **6**, 15–50 (1996).
47. Perdew, J. P., Burke, K. & Ernzerhof, M. Generalized gradient approximation made simple. *Phys. Rev. Lett.* **77**, 3865 (1996).

48. Monkhorst, H. J. & Pack, J. D. Special points for Brillouin-zone integrations. *Phys. Rev. B* **13**, 5188 (1976).
49. Henkelman, G., Uberuaga, B. P. & Jónsson, H. A climbing image nudged elastic band method for finding saddle points and minimum energy paths. *J. Chem. Phys.* **113**, 9901–9904 (2000).
50. Mao, H., Xu, J.-A. & Bell, P. Calibration of the ruby pressure gauge to 800 kbar under quasi-hydrostatic conditions. *Geophys Res Solid Earth* **91**, 4673–4676 (1986).

Acknowledgements

We thank H. K. Mao (Center for High-Pressure Science and Technology Advanced Research, Shanghai), H. L. Dong (Center for High Pressure Science and Technology Advanced Research, Shanghai), and B. Liu (Yanshan University) for valuable discussions; C. X. Zhu (Shanghai Institute of Ceramics, Chinese Academy of Sciences) for assistance with the HAADF-STEM characterizations. This work was supported by the Science and Technology Commission of Shanghai Municipality (Nos. 22ZR142330 (G.L.) and 21DZ1208900 (X.L.)), the National Key Research and Development Program of China (Nos. 2023YFB3712401 (X.L.) and 2022YFC2906100 (X.Z.)), the National Natural Science Foundation of China (Nos. 52004157 (G.L.), 52334009 (X.L.), 52374307 (X.Z.) and 52304331 (Z.P.)), the Innovation Program of Shanghai Municipal Education Commission (No. 2023ZKZD48 (X.Z.)), the "Shuguang Program" supported by the Shanghai Education Development Foundation and the Shanghai Municipal Education Commission (No. 21SG42 (X.Z.)).

Author contributions

G.L., X.X., X.Z., and X.L. conceived the project. P.Z., P.C., C.Su., Z.P. set up and performed the experiments. X.X. performed the theoretical calculations. H.C., C.Sh., X.Y., and Q.X. participated in discussions. P.Z. wrote the manuscript with inputs from other authors. G.L. and X.Z. contributed to the revision of the manuscript.

Competing interests

The authors declare no competing interests.

Additional information

Supplementary information The online version contains supplementary material available at https://doi.org/10.1038/s41467-025-57604-0.

Correspondence and requests for materials should be addressed to Guangshi Li, Xiaolu Xiong, Xingli Zou or Xionggang Lu.

Peer review information *Nature Communications* thanks Liang Zuo and the other, anonymous, reviewer(s) for their contribution to the peer review of this work. A peer review file is available.